

Structural and electrical investigation of MI₂M and MI₃M diodes for improved non-linear, low bias rectification

I. Nemr Nouredine^{1,†}, N. Sedghi¹, J.S. Wrench^{2,*}, I. Z. Mitrovic¹, P.R. Chalker², S. Hall^{1,†}

¹*Department of Electrical Engineering and Electronics, University of Liverpool, Brownlow Hill, L69 3GJ Liverpool, UK*

²*School of Engineering, University of Liverpool, Ashton Street, Liverpool L69 3GH, UK*

[†]*Corresponding authors: ibbe85@gmail.com; shall@liverpool.ac.uk*

*Current address: * MDP Co., Applied Materials, UK*

Keywords: multi-dielectric diode, native oxide, tunnelling, Tsu-Esaki model, transfer matrix method, WKB approximation, THz rectification, rectenna

Multi-stack metal-insulator-metal diodes devices of atomic layer deposited (ALD) and sputtered Ta₂O₅ and Al₂O₃ dielectrics with Au bottom electrode are investigated comprehensively by experiment and modelling. The layer structure is inspected - and the native contact metal oxide effects are incorporated in the modelling computation - using atomic force microscopy (AFM), spectroscopic ellipsometry, and transmission electron spectroscopy (TEM). The tunnelling transport is successfully modelled using both the transfer matrix (TMM) and Wentzel-Kramers-Brillouin (WKB) methods. Parasitic currents are identified using their voltage and temperature dependence. Rectification for a triple dielectric layer device is shown to occur at a turn-on voltage as low as 170 mV with a non-linearity of 3 and an asymmetry increasing from 2.2 at the turn-on voltage to over two orders of magnitude at 1 V.

1. Introduction

Terahertz (THz) rectification is required for the development of rectennas used for scavenging thermal infrared radiation, imaging by detection of hot object emissions, or even solar energy harvesting.^{1,2} Rectennas can be used for wireless THz communication, particularly satellites, with large bandwidth potential (up to 100 GHz) for data transfers exceeding 1 Gb/s. They could also be used in detectors for THz imaging in biomedical applications,³ skin cancer detection,⁴ and even passive imaging.⁵ A distinct advantage over solar cells is the capability of recycling residual heat from small electronic devices, combustion engines, or even large industrial machinery.⁶ The potential of rectennas to operate at higher IR/THz frequencies has been hindered by the lack of a diode nanostructure that can work efficiently when coupled to an antenna.⁷ Metal-insulator-metal (MIM) tunnelling diodes have potential for thermal and solar energy conversion.^{8,9} There are indications of their potential for THz rectification,¹⁰⁻¹² specifically for THz rectenna integration,¹³ with the capability of engineering their rectifying performance with double dielectric structures.¹⁴ Rectification is attained via femtosecond-speed tunnelling¹⁵ at sufficiently low turn-on voltage, ideally towards zero bias,¹⁶ which is required for efficient operation in low-power applications such as IR/THz rectenna arrays.^{17,18}

We previously reported tunnelling mechanisms in thickness-stepped MIIM structures.¹⁹ We investigate in this work the influence of band gap engineering of the structures on the rectifying performance and focus on experiment-to-model matching, reporting well-defined rectification at low turn-on voltage.

The rectifying characteristics of the diodes containing Ta₂O₅ and Al₂O₃ are analysed in terms of asymmetry, linearity, dynamic resistance and a defined turn-on voltage (V_{ON}) of the current voltage (IV) measurements. According to these characteristics, the performance of relevant MIM/MIIM work is assessed. While Cu/0.7nm-CuO/Au structure has shown low dynamic resistance in the order of 100 Ω with 67² nm² size, which is suitable for THz applications, it suffers from very low non-linearity and low |0.1| V voltage range.²⁰ Another THz device, 60² nm² poly-Si/1.38nm-SiO₂/poly-Si, shows better non-linearity but a low |0.15| V voltage range and large R_d of the order 10⁸ Ω .²¹ A larger size 20² μ m² Ni/NiOx/ZnO/Cr structure showed sufficient non-linearity but low |0.5| V voltage range and large R_d in the order of 10⁸ Ω .²¹ A ZCAN/2.5nm-Al₂O₃/2.5nm-Ta₂O₅/Al structure achieved good non-linearity, low turn-on voltage of 0.2 V, and |1.2| V voltage range but large R_d in the order of 10⁷ Ω .²² Other relevant reported devices suffer from low non-linearity.^{17,23,24} Further overview of dielectric based rectifiers is given elsewhere,²⁵ where the choice

of the oxide for effective integration into infrared rectennas is discussed.

2. Fabrication

Table 1 shows structural details of the fabricated samples with area dimensions of $100 \times 100 \mu\text{m}^2$ for all. We consider four MI_nM devices (where n is the number of insulator layers) in addition to an MIM, sample (S5), which was used for transmission electron microscopy (TEM) imaging. Corning glass substrates were cleaned using diluted Decon-90, acetone, and isopropanol, and blown dry with nitrogen. Si substrates, of 2 nm thick native oxide, were cleaned with isopropanol and blown dry with nitrogen. The thicknesses of the dielectric layers were measured by variable angle spectroscopic ellipsometry using a *M2000U J.A. Woollam Co., Inc.* instrument. The IV measurements were done in the dark using an *Agilent B1500 Analyzer* on a temperature-controlled heating stage or in a cryostat with liquid nitrogen cooling. Voltage was swept with 10 mV step size at a settling time of 0.3 s from 0 V to negative or positive bias. The top and the bottom metal films were deposited using a *Moorfield* thermal evaporator. Metals of high purity (99.999% Al, 99.9% Cr, 99.9985% Au) were cleaned and evaporated upwards at a pressure of 5×10^{-7} Torr reaching the rotating samples at a rate of 4 Å/s. The electrodes were patterned by a lift-off photolithographic process for all devices [FIG. 1(a)] using 1.2 μm thick *Shipley S1813* positive photoresist.

Table 1. Device structures and layer thicknesses.

S.	t	M ₁	I _{NO1}	dep.	t	I ₁	t	I ₂	I _{NO2}	t	M ₂	
S1	80	Au	–	Sp.	4	Ta ₂ O ₅	1	Al ₂ O ₃	AlO _x	80	Al	
S2	80	Au	–	Sp.	0.5	Al ₂ O ₃	4	Ta ₂ O ₅	AlO _x	80	Al	
S3	CG	80	Au	–	ALD	4	Ta ₂ O ₅	1	Al ₂ O ₃	AlO _x	80	Al
S4	Si	80	Au	–	Sp.	6	Ta ₂ O ₅	–	–	20/60	Cr/Au	
S5	Si	120	Al	AlO _x	Sp.	1	Al ₂ O ₃	4	Ta ₂ O ₅	AlO _x	120	Al

t: thickness [nm], S.: substrate, CG: corning glass, M₁/M₂: bottom/top metal, I₁/I₂: 1st/2nd insulator, dep.: deposition technique for I₁/I₂, Sp.: sputtered, I_{NO1}/I_{NO2}: native oxides for M₁/M₂

The Al₂O₃ and Ta₂O₅ films were deposited for samples S1 and S2 using radio frequency (RF) sputtering at room temperature at a power of 45 W and at an argon flow rate of 0.5 sccm. The Al₂O₃ and Ta₂O₅ layers were sputtered using two separate targets in the chamber at a rate of 0.095 Å/s and 0.54 Å/s respectively. The thicknesses were verified on Si substrates using spectroscopic ellipsometry. Atomic layer deposition (ALD) was used to deposit the oxides for sample S3. ALD was done at a temperature of 200 °C using precursors tantalum ethoxide for Ta₂O₅ and trimethylaluminum (TMA) for Al₂O₃, and deionized water as the oxidant agent. While the purge time was 10 s for all precursors, the pulse time was 0.02/0.04 s for TMA/H₂O used for Al₂O₃ and 0.2/0.04 s for

Ta(O)₅/H₂O used for Ta₂O₅. The sample set is selected with inert Au as the bottom electrode to avoid the growth of native oxide; 2-4 nm of native oxide (AlO_x) is reported to grow above Al in several hours.²⁶ This is in addition to the low measured surface roughness of Au (0.44 nm) as compared to Al (2.4 nm), critical for tunnelling, as depicted in FIG. 1(a). The layer structure for sample S5 is imaged using high resolution (HR)-TEM [FIG. 1(b)], which shows thick AlO_x layers grown at the interfaces with Al electrodes: 3 nm above the bottom Al, and surprisingly 3 nm below the top Al. This additional AlO_x layer is taken into account in the modelling. Assuming AlO_x as Al₂O₃, the structures shown in FIG. 1(c) can be classified as: MIM S4, MI₂M S1 and S3, and MI₃M S2.

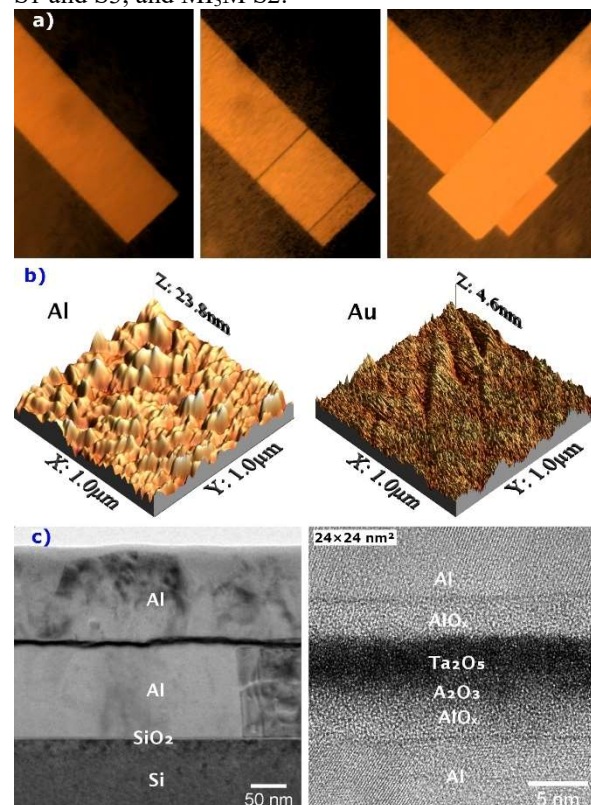


FIG. 1. a) Microscope images of device fabrication process using lift-off photolithography: after deposition of M1, after photoresist development, and after deposition of M2 (respectively from left to right). b) AFM images of Al and Au metal electrodes. c) HR-TEM images of S5: the layer structure and $24 \times 24 \text{ nm}^2$ of the active area showing AlO_x layer below the top Al and on top of the bottom Al in addition to the sputtered Al₂O₃/Ta₂O₅ oxide stack.

3. Tunnelling model

Modelling is used both in the design and experimental evaluation of the diodes. It is based on the Tsu-Esaki method²⁷ and has been modified as follows based on previous reported work.^{28,29} The tunnelling current is calculated using a piecewise transfer matrix method (TMM), applicable for multi-barrier tunnelling diodes. The electron is described by a wave function which is damped by the classically forbidden energy barriers within the dielectric stack. Each barrier is divided into N slices (FIG. 2), where the wave function and its derivative are assumed to be continuous at the boundary of each slice.

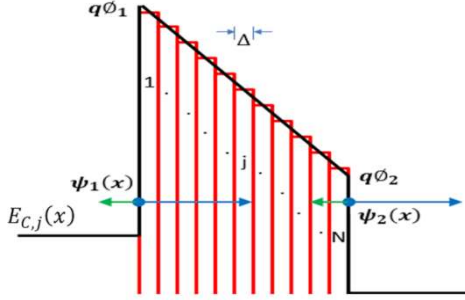


FIG. 2. N -sliced energy barrier of a single-layer dielectric. The electron of constant mass m_j is transferred as a wave function dropping exponentially till reaching the interface with M_2 of occupation state $\psi_2(x)$.

The transmission coefficient is the ratio of the current reaching the second electrode to that at the first electrode:

$$T(E_x) = \frac{J_N}{J_1} = \frac{k_N m_N |A_N|^2}{k_1 m_1 |A_1|^2} \quad (1)$$

A_1 and A_N are the wave amplitudes at the dielectric interfaces with M_1 and M_2 respectively.

At each value of voltage bias, the position of the conduction band $E_{C,j}(x)$ is calculated taking into consideration the image force effect which lowers the barrier defined by the work function.³⁰ The energy, E_x is discretized, and the probability $T(E_x)$ for each is found using:

$$k_j = \sqrt{2m_j[E_x - E_{C,j}(x)]}/\hbar \quad (2)$$

and TMM approach, considering a piecewise constant potential.³¹

For faster computation of $T(E_x)$, the Wentzel-Kramers-Brillouin (WKB) approximation is adopted. Substituting the wave function in the time-independent Schrödinger equation³² and using the following approximation,

$$T_{WKB}(E_x) = \exp\left(-\frac{2}{\hbar} \int_0^{x_1} \sqrt{2m_{ox}(E_C - E_x)} dx\right) \quad (3)$$

the total tunnelling current density is found for each voltage bias as the difference of charge transport flowing from M_1 electrode to M_2 electrode $J_{M_1-M_2}$ and that flowing in the opposite direction $J_{M_2-M_1}$ such that the total tunnelling current density is:

$$\begin{aligned} J &= |J_{M_1-M_2} - J_{M_2-M_1}| \\ &= (4\pi m q / h^3) \int_{E_{min}}^{E_{max}} T(E_x) dE_x \int_0^\infty [f_1(E) \\ &\quad - f_2(E)] dE_\rho \end{aligned} \quad (4)$$

where $T(E_x)$ is the transmission probability. $f_1(E)$ and $f_2(E)$ are the energy distribution functions representing the probability of occupation of states near the dielectric interfaces with M_1 and M_2 respectively. The energies, E_{min} and E_{max} are the highest conduction band edges of the two electrodes and the dielectric respectively. $\int_0^\infty [f_1(E) - f_2(E)] dE_\rho$ is the difference in the supply of electrons at the dielectric interfaces. dE_x is the energy segment taken by specifying certain number of states included between the lower and upper limits. The probability that a particle will have energy E is described by the Fermi-Dirac energy distribution function at thermal equilibrium:

$$f(E) = \frac{1}{1 + \exp\left(\frac{E_x + E_\rho - E_f}{k_B T}\right)} \quad (5)$$

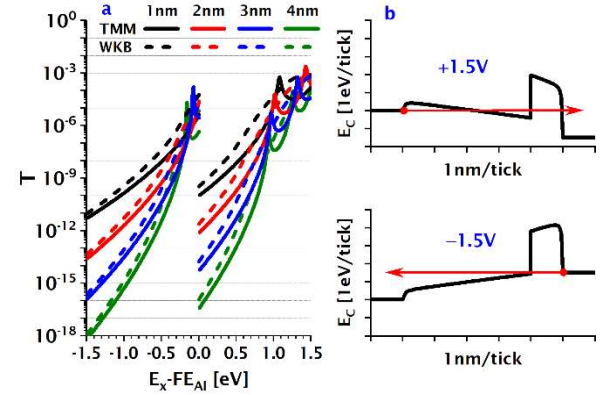


FIG. 3. a) TMM- and WKB-modelled transmission probability T of Al/Al₂O₃/Ta₂O₅/Al, considering 1 nm thick Al₂O₃ while varying Ta₂O₅ thickness: 2, 3, 4, and 5 nm, at +1.5 V (left) and -1.5 V (right). b) The corresponding conduction band diagrams, where the electron injection is indicated by the red arrow.

Using the model with TMM and WKB approaches, the structures are first optimised for larger transmission probability (FIG. 3). The model takes into account the tunnelling peaks. While these peaks considerably enhance the current, their predictable occurrence at these large voltages is undesirable for practical use in

low-power and passive applications, which is an objective for this work.

4. Diode design

For sufficient rectification, we focus on realising (a) larger asymmetry, defined as the ratio of the current at positive bias to that at negative bias at certain voltage: $f_{asym} = J_+/J_-$ (b) lower dynamic resistance, defined as: $R_d = dV/dI$, and (c) larger non-linearity, defined as the ratio of the static to dynamic resistance: $f_{NL} = (V/J)/(dV/dJ)$. The onset voltage is defined as the voltage at which the current increases abruptly, which could happen in a diode at one or both polarities. A turn-on voltage (V_{ON}) is defined as the point at which the current becomes large enough at one polarity to create $f_{asym} = 3$ which is considered sufficient for THz applications.¹⁷ V_{ON} was elsewhere defined as the transition from linearity ($f_{NL}=1$) to non-linearity ($f_{NL}>1$).³³ The aim is for rectification at the lowest possible V_{ON} , critical for passive operation in energy harvesting devices such as rectennas.

The conduction band $E_C(x)$ diagrams serve to illustrate the tunnelling paths in the device structures (FIG. 4), (note that the arrows do not correspond to the actual path of electron transport as they will drift in the conduction band). At each applied voltage, a major factor for increasing the tunnelling probability is described by altering the shape of $E_C(x)$ to minimize the effective tunnelling distance: thinner oxides and lower barrier height. To create an asymmetry, the structure is engineered for the effective tunnelling distance, energy band bending and barrier heights, to be larger at one polarity, e.g. larger at $-1.5/-0.5$ V as compared to $+1.5/+0.5$ V for S1 and S2. While this can only be obtained by increasing the work function dissimilarity of the electrodes in MIM structures, much larger asymmetry can be achieved in multi-stack dielectric structures by tuning the individual thickness of the dielectric layers. The use of two or more barriers serves to limit the dominance of thermal emission and could bring further enhancement in f_{NL} with step and resonant tunnelling, which is desirable for THz rectification. Fowler-Nordheim tunnelling (FNT) could dominate where band bending shortens the effective distance for electrons to tunnel, and step tunnelling (ST) is reached when the band bending is steep enough (S1 at $+1.5$ V).³⁴ Resonant tunnelling (RT) arises from charge transport via intermediate bound states in the quantum well between two dielectrics as the electron energy is matched with one of them (S2 at -1.5 and $+1.5$ V).²⁹

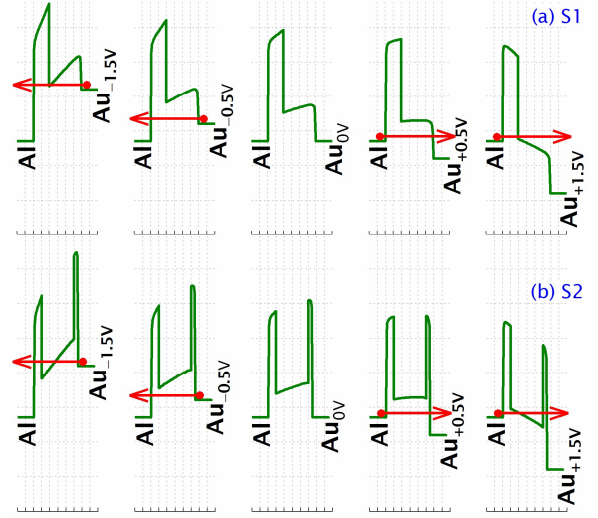


FIG. 4. Conduction band diagrams of S1 (a) and S2 (b) structures at -1.5 , -0.5 , 0 , $+0.5$, and $+1.5$ V where Al left electrode is grounded. Electron injection is indicated by the red arrow. Each x-axis tick corresponds to 1 nm. All axes set to the same scale.

5. Results and discussion

5.1 Rectifying performance

The experimental characteristics and the key rectification parameters are shown in FIG. 5 and summarised in Table 2. While S4 has the lowest R_d , it shows poor rectifying performance at low bias with f_{NL} of 3 obtained at V_{ON} of 0.84 V and low f_{asym} not exceeding 4.2. Despite having a similar structure, the ALD-S3 achieves sufficient rectification at an order of magnitude larger R_d and at almost double V_{ON} of sputtered-S1, which makes the latter superior. Due to its lower R_d and slightly larger f_{asym} at its lower V_{ON} , S2 shows better low voltage rectifying performance than S1. Its close-to-zero V_{ON} value (0.17 V) associated with well-defined rectification (f_{NL} of 3 increasing towards 8.8 at 0.69 V and f_{asym} of 2.2 increasing towards 133 at 1.14 V) is distinguished as compared to other state-of-the-art tunnelling rectifiers. An MIM device, demonstrated for zero-bias rectification at 28.3 THz, shows poor rectifying characteristics over small voltage range $|V|<0.4$ V estimating f_{asym} close to 1 and $f_{NL} < 2$ (Ref³⁵). Using our definition of V_{ON} corresponding to f_{NL} of 3, we estimate the values from IV graphs in different studies as follows. The lowest recorded V_{ON} for tunnelling rectifiers is estimated to be ~ 0.12 V³⁶ and ~ 0.17 V³⁷ for MIM devices. However, both were applied to smaller voltage range of $|V| \leq 0.15$ V and 0.3 V respectively as compared to 1.4 V for S2. Low V_{ON} can also be estimated in other studies: ~ 0.2 V³⁸ and ~ 0.25 V²¹ for MIIM and ~ 0.4 V³⁹ and ~ 0.5 V⁴⁰ for MIM.

Table 2. Rectifying parameters of the devices extracted at V_{ON} .

Device	Structure	V_{ON}	f_{NL}	f_{asym}	R_d [Ω]
S1	Ml ₂ M	0.21	3	1.7	7×10^9
S2	Ml ₃ M	0.17	3	2.2	5×10^8
S3	Ml ₂ M	0.33	3	2.3	7×10^{10}
S4	MIM	0.84	3	2.1	2×10^6

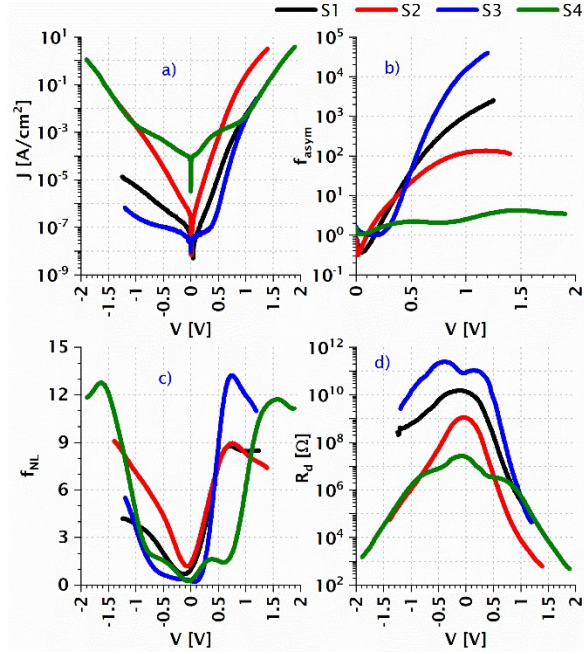


FIG. 5. Rectifying characteristics of the devices at 300 K: (a) JV curves, (b) f_{asym} , (c) f_{NL} , and R_d .

5.2 Modelling of experimental results

Simulations are compared to the experimental JV characteristics [FIG. 6(a,b)]. The calculations assume respectively, work functions of 4.28,⁴¹ 4.4,⁴² and 4.9 (Ref. ⁴³) for Al, Cr, and Au, Fermi energy FE of 11.7 eV for Al,⁴⁴ an electron affinity (E_a) of 1.35 and 3.75 eV for Al₂O₃ and Ta₂O₅,⁴⁵ and a dielectric constant of 10 (Ref. ⁴⁶) and 25 (Ref. ⁴⁷) for Al₂O₃ and Ta₂O₅. The best experimental-to-model fittings have been made considering an additional 1 nm layer of Al₂O₃ below the top Al layer [FIG. 1(c)]. As compared to the 3 nm reported using HR-TEM, the difference can be explained by possible further oxidation by the coating used for HR-TEM sample preparation.⁴⁸ An effective mass coefficient of electrons is used in fittings: 1 in the metals and 0.18 and 0.2 in the insulators of S1 and S2 respectively. For S1 and S2, WKB and TMM current calculations are nicely matched over the applied voltage range [FIG. 6(a,b)]. This is because RT and ST mechanisms of large energy barrier variation leading to inaccuracy in WKB, are unlikely to occur within the voltage range. Major negative peaks before negative differential resistance (NDR) are accounted for

calculating the tunnelling transmission probability $T(E_x)$ using TMM but not in the WKB method [FIG. 6(c,d)]. The TMM model predicts the currents have the first resonance peaks before NDR at -3.6 V for S1 and at $-1.9/+1.6$ V for S2 [FIG. 6(c,d)]. TMM also predicts smaller NDR peaks for step tunnelling for S1, starting at $+1.5$ V. The current rise is noticeably steep in positive bias for S1 and S2 [FIG. 6(a,b)]. This is explained for S1 by the lower conduction band, which bends steeply shortening the effective tunnel distance for electrons to reach step tunnelling at $+1.5$ V [FIG. 4(a)]. For S2, the potential well becomes wide and deep enough for resonant tunnelling to occur at $+1.6$ V for S2 [FIG. 4(b)]. The steeper current rise at negative bias for S2 as compared to S1 is explained by the shorter effective tunnel distance in the former (FIG. 4), where the conduction band is lower. Moreover, as the negative bias is increased, the conduction band of S2 as compared to S1 bends steeper towards wider and deeper resonance potential well [FIG. 4] for earlier occurrence of RT at -1.9 V for S2 as compared to -3.6 V for S1 [FIG. 6(c,d)]. It should be noted that the voltage regime of the J-V measurements could not be exceeded due to the onset of breakdown, which is a common obstacle to achieving RT.

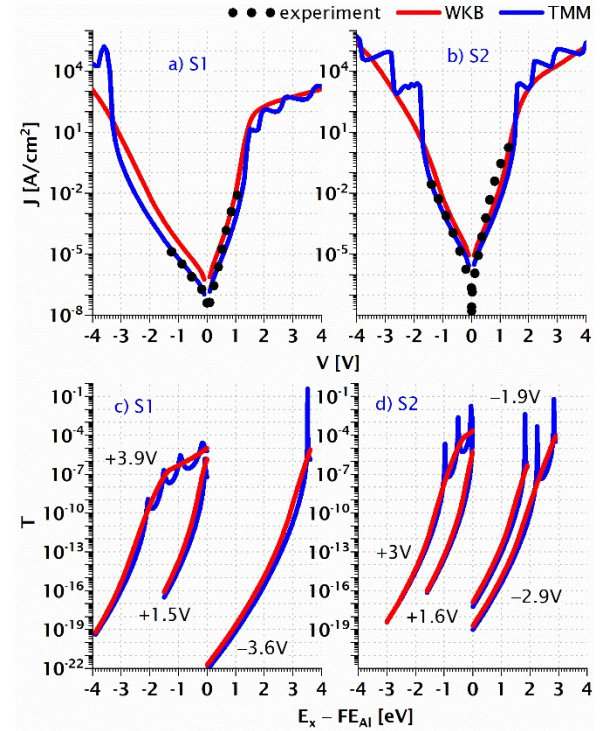


FIG. 6. Experimental versus WKB/TMM modelled JV curves of S1 (a) and S2 (b) at 300 K and their corresponding $T(E_x - FE_{Al})$ at voltages of selected peaks (c,d).

The conduction mechanisms are further investigated using the JV temperature sensitivity (FIG. 7). Poole-Frenkel emission (PFE) is bulk limited,⁴⁹ and this implies that temperature sensitivity would be essentially the same at both polarities. Since this was not observed, the domination of PFE is unlikely for S1, S2, and S3. Defect enhanced direct tunnelling,³⁸ where the electrons are transported via PFE or trap-assisted tunnelling across Ta₂O₅, followed by direct tunnelling across the thinner Al₂O₃, is unlikely. This is because it predicts steeper current rise for both, S1 at negative bias and S2 at negative bias, which is not experimentally observed. Tunnelling is firstly pointed out by the current upsurge occurring for S3 at 77 K, low enough temperature for thermal emission to become effectively frozen out. Matching with the model and the minor temperature sensitivity at negative bias for S1 and S2 are further indications of the predominance of tunnelling. At $V > V_{ON}$, a slight mismatch with the model becomes more visible where the experimental data shows a slightly steeper increase in the current than that predicted by the tunnelling model. This divergence from TMM/WKB curves is larger for S2 as compared to S1, which is consistent with larger temperature dependence of S2 (at $V > V_{ON}$). Consequently, the suggestion of some thermal emission besides tunnelling holds strongly, and this applies generally to all devices.

For the 6 nm-Ta₂O₅ MIM S4, Schottky emission (SE) and PFE dominate over $|0.2-1|$ V and $|1-1.9|$ V ranges at both polarities respectively with dynamic relative permittivity ϵ_r of 5.2 and trap depth ϕ_T of 1.2 eV. These values extracted using the JV data at 300 K are consistent with literature values of 4.6-5.8^{50,51} and 0.58-2.2 eV⁵²⁻⁵⁴ respectively. The SE mechanism is also taken into consideration for other MI₂M/MI₃M devices of similar fabrication conditions (S1, S2). Accordingly, considering possible larger electron affinity E_a of the native AlO_x (e.g. 2.58 eV⁵⁵ as compared to 1.35 eV of Al₂O₃), it becomes feasible for electrons at the interface between Al electrode and the native oxide to cross the barrier via SE at $V > 0.6$ V [FIG. 8(a)]. This is predicted for S2 but not likely for S1 with large adjacent Al₂O₃ barrier. Therefore, for S2, the electron transport is via SE followed by direct tunnelling across a shorter effective tunnelling distance which could explain the temperature-sensitive current boost in this voltage regime [FIG. 6(b)]. Besides, for S3, the existence of larger number of defects in the ALD-deposited Ta₂O₅ bulk is indicated by the steady JV temperature sensitivity along the applied range [FIG. 7(c)], the larger offset in its V_{ON} (Table 2), and its much larger hysteresis around 0 V (negative versus positive sweeps) as compared to the sputtered devices [FIG. 8(b)].

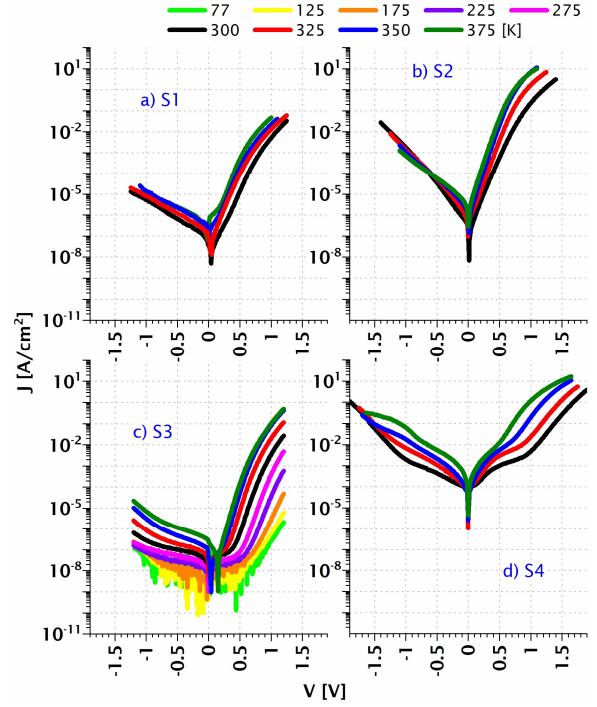


FIG. 7. Temperature dependent JV curves of the devices (same axes scale for all) measured using heating stage at 300-to-375 K (a,b,d) or using the cryostat at 77-to-375 K (c).

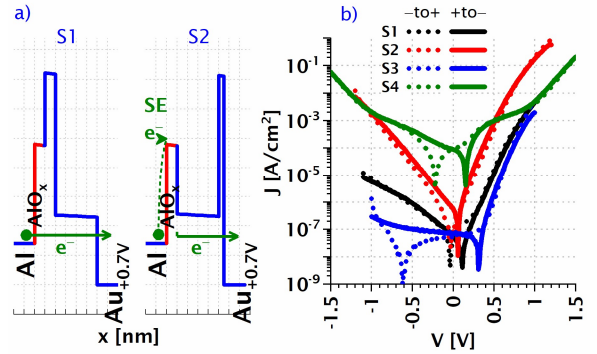


FIG. 8. a) Conduction band diagrams of S1 and S2 at +0.7 V considering AlO_x of lower E_a which enhances SE for S2 (green arrow), b) JV curves swept from maximum negative voltage to maximum positive voltage (positive sweep) and vice versa (negative sweep).

5.3. Performance assessment of area minimisation

The minimisation of the device active area is required in order to increase the cut-off frequency for rectification at higher frequencies. Its effect on the device rectifying performance is investigated on S4 structure, varying its active area from 20×20 till $250 \times 250 \mu\text{m}^2$ (FIG. 9). As the active area is minimized, the current and f_{NL} drop while R_d increases. This consistent slight performance variation can be explained by the high resistivity of the Cr metal line, since it is directly proportional to the resistivity characteristic ρ of the metal ($100 \times 10^{-8} \Omega\text{m}$ for Cr). As the active area is minimised, the current in its Cr/Au electrode is impeded by the largely resistive metal (Cr). The results are in agreement with another study¹⁷ showing significantly lower nonlinearity and higher zero-bias impedance with Cr/Au MIM structures fabricated at nanoscale as compared to those at microscale. This consideration becomes crucial for THz nanostructures, and the choice of the much less resistive Au/Al ($\rho = 2.44/2.65 \times 10^{-8} \Omega\text{m}$) for the other devices (S1, S2, S3) serves for rule out this advantage when area is minimised for better integration into high frequency THz/infrared applications.

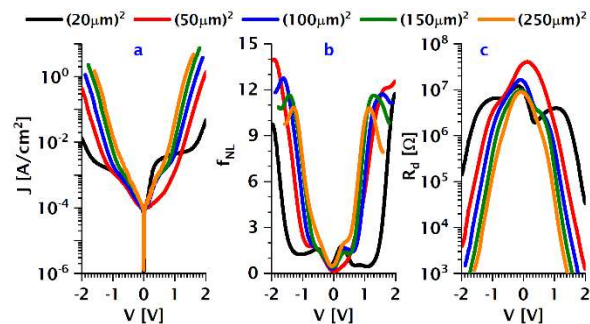


FIG. 9. JV curves for S4 structure fabricated at the same fabrication procedure and conditions, but with varied active area: from 20×20 till $250 \times 250 \mu\text{m}^2$.

6. Conclusion

MIM diodes of ultra-thin Al_2O_3 and Ta_2O_5 layers have been designed, fabricated and characterised with the aim to investigate non-linear rectification at lower V_{ON} . The consistency of the experimental characteristics with the tunnelling transmission probability has been demonstrated and analysed in terms of the dominant conduction mechanisms. The dominance of tunnelling is evident from the sharp current rise at the voltage onset at 77 K and matching with the adapted Tsu-Esaki model calculations using TMM and WKB schemes. Temperature sensitivity is discussed where it is suggested that SE mechanisms are unlikely to play a significant role. The MIM device (S2) with sputtered oxides, was seen to show the closest-to-zero rectifying performance: a non-linearity of 3 occurring at V_{ON} of 0.17 V with an asymmetry of 2.1 increasing towards

10^2 scale at 1 V. This work demonstrates the capability of multi-insulator tunnelling devices to achieve enhanced, non-linear rectification at lower voltages for passive ultra-high speed applications in the THz regime.

Acknowledgements

This work was funded partly by EPSRC UK, project reference EP/K018930/1. The author acknowledges the *University of Liverpool* and *National Tsing Hua University* for provision of a studentship.

References

- ¹R. Bailey, *Journal of Engineering for Gas Turbines and Power* **94** (2) 73 (1972)
- ²Y. Huang and S. Hall and Y. Shen, UK Patent No. 2484526 (A) (2012).
- ³X. Yin et al., *Terahertz Imaging for Biomedical Applications : Pattern Recognition and Tomographic Reconstruction*. (Springer, New York, 2012).
- ⁴R. Woodward et al., *Journal of Investigative Dermatology* **120** (1) 72 (2003)
- ⁵M. Kowalski and M. Kastek, *IEEE Transactions on Information Forensics and Security* **11** (9) 2028 (2016)
- ⁶S. May, "Stealing the heat" in *Gendercide* (The Economist, 2010), Vol. Technology Quarterly.
- ⁷I. Nemr Nouredine, *Resonant tunnelling nanostructures for THz energy harvesting*, University of Liverpool (2018).
- ⁸M. Dagenais et al., *Solar spectrum rectification using nano-antennas and tunneling diodes*, *Optoelectronic Integrated Circuits XII* (01/01/2010).
- ⁹S. Bhansali et al., *Tunnel Junction based Rectenna-A Key to Ultrahigh Efficiency Solar/Thermal Energy Conversion*, AIP Conference Proceedings.
- ¹⁰M. Feiginov et al., *Applied Physics Letters* **104** (24) 243509 (2014)
- ¹¹T. Sollner et al., *Applied Physics Letters* **43** (6) 588 (1983)
- ¹²T. Kang et al., *Nature communications* **9** (1) 1 (2018)
- ¹³G. Jayaswal et al., presented at the 2018 IEEE/MTT-S International Microwave Symposium-IMS, 2018 (unpublished).
- ¹⁴S. Grover and G. Model, *Solid State Electronics* **67** (1) 94 (2012)
- ¹⁵E. Hauge and J. Støvneng, *Reviews of Modern Physics* **61** (4) 917 (1989)
- ¹⁶N. Sedghi et al., *Zero Bias Resonant Tunnelling Diode for Use in THz Rectenna*, 18th Workshop on Dielectrics in Microelectronics, Cork, Ireland (9-11 June 2014).
- ¹⁷B. Berland, *Photovoltaic Technologies Beyond the Horizon: Optical Rectenna Solar Cell*, NREL/SR-520-33263, ITN Energy Systems, Inc. (2003).

- ¹⁸Naser Sedghi et al., presented at the 2013 Proceedings of the European Solid-State Device Research Conference (ESSDERC), 2013 (unpublished).
- ¹⁹I. Nemr Noureddine et al., Journal of Vacuum Science and Technology B: Nanotechnology and Microelectronics **35** (1) (2017)
- ²⁰M. N. Gadalla et al., Scientific Reports **4** (2014)
- ²¹A. Singh et al., Applied Surface Science **334** 197 (2015)
- ²²N. Alimardani et al., Journal of Applied Physics **116** (2) 024508 (2014)
- ²³S. Zhang et al., ECS Solid State Letters **2** (1) 416 (2013)
- ²⁴S. Krishnan et al., Sensors and Actuators A: Physical **142** (1) 40 (2008)
- ²⁵Ivona Z. Mitrovic et al., Materials **14** (18) 5218 (2021)
- ²⁶K. Wefers and C. Misra, *Oxides and hydroxides of aluminum*, (1987).
- ²⁷R. Tsu and L. Esaki, Applied Physics Letters **22** (11) 562 (1973)
- ²⁸Z. Wang et al., Journal of Vacuum Science & Technology B **31** (2) (2013) 021209
- ²⁹N. Sedghi et al., Applied Physics Letters **102** (9) (2013) 092103
- ³⁰J. Simmons, Journal of Applied Physics **34** (6) 1793 (1963)
- ³¹O. Probst, American Journal of Physics **70** (11) 1110 (2002)
- ³²E. Schrödinger, Annalen der Physik **384** (4) 361 (1926)
- ³³A. Hoofring et al., Journal of Applied Physics **66** (1) 430 (1989)
- ³⁴N. Alimardani and J. Conley, Applied Physics Letters **102** (14) 143501 (2013)
- ³⁵G. Jayaswal et al., Materials today energy **7** 1 (2018)
- ³⁶K. Choi et al., IEEE Electron Device Letters **31** (8) 809 (2010)
- ³⁷P. Esfandiari et al., *Tunable antenna-coupled metal-oxide-metal (MOM) uncooled IR detector*. (SPIE, 2005).
- ³⁸N. Alimardani and J. Conley, Applied Physics Letters **105** (8) 082902 (2014)
- ³⁹F. García de Arquer et al., *Engineering the Input Impedance of Optical Nano Dipole Antennas: Materials, Geometry and Excitation Effect*. (2011), pp.3144.
- ⁴⁰C. Zhuang et al., ECS Solid State Letters **4** (5) P39 (2015)
- ⁴¹T. Drummond, *Work functions of the transition metals and metal silicides*, Sandia National Labs., Albuquerque, NM (US); Sandia National Labs ... (1999).
- ⁴²C. Smithells et al., *Smithells Metals Reference Book*, 8th ed. (Elsevier Butterworth-Heinemann, Amsterdam, 2004), pp.18.
- ⁴³N. Szydlo and R. Poirier, Journal of Applied Physics **51** (6) 3310 (1980)
- ⁴⁴S. Hüfner, *Photoelectron spectroscopy: principles and applications*. (Springer Science & Business Media, 2013).
- ⁴⁵R. Southwick et al., IEEE Transactions on Device and Materials Reliability **11** (2) 236 (2011)
- ⁴⁶D. Buchanan et al., International Electron Devices Meeting 2000, Technical Digest 223 (2000)
- ⁴⁷K. Kukli et al., J Electrochem Soc **142** (5) 1670 (1995)
- ⁴⁸S. Abolhassani and P. Gasser, Journal of microscopy **223** (1) 73 (2006)
- ⁴⁹J. Frenkel, Physical Review **54** (8) 647 (1938)
- ⁵⁰K. Kukli et al., Journal of Crystal Growth **212** (3) 459 (2000)
- ⁵¹N. Alimardani et al., Journal of Applied Physics **116** (2) 024508 (2014)
- ⁵²J. Thomas III, Applied Physics Letters **22** (8) 406 (1973)
- ⁵³M. Houssa et al., Journal of Applied Physics **87** (12) 8615 (2000)
- ⁵⁴G. Alers et al., Applied Physics Letters **72** (11) 1308 (1998)
- ⁵⁵ML. Huang et al., Applied physics letters **89** (1) 012903 (2006)